

1           **Precipitation of protodolomite facilitated by sulfate-reducing bacteria:**

2                   **The role of capsule extracellular polymeric substances**

3  
4   Deng Liu<sup>1,2,\*</sup>, Qigao Fan<sup>2</sup>, Dominic Papineau<sup>1,3,4,5</sup>, Na Yu<sup>2</sup>, Yueying Chu<sup>6</sup>, Hongmei Wang<sup>1,</sup>

5                                   <sup>2</sup>, Xuan Qiu<sup>1</sup> and Xingjie Wang<sup>7</sup>

6  
7           <sup>1</sup>State Key Laboratory of Biogeology and Environmental Geology, China University of

8                                   Geosciences, Wuhan 430074, China

9           <sup>2</sup>School of Environmental Studies, China University of Geosciences, Wuhan 430074, China

10           <sup>3</sup>London Centre for nanotechnology, University College London, 17-19 Gordon Street,

11                                   London, UK

12           <sup>4</sup>Department of Earth Sciences, University College London, London, UK

13           <sup>5</sup>Center for Planetary Sciences, University College London, London, UK

14           <sup>6</sup>State Key Laboratory of Magnetic Resonance and Atomic and Molecular Physics, Wuhan

15           Institute of Physics and Mathematics, Chinese Academy of Sciences, Wuhan 430071, China

16           <sup>7</sup>School of Resource and Environmental Engineering, Wuhan University of Science and

17                                   Technology, Wuhan 430081, China

18  
19                                   Corresponding author: Deng Liu (liud\_cug@126.com)

20                                   *Chemical Geology*

21  
22                                   November 17, 2019

23 **ABSTRACT**

24 The origin of dolomite has long puzzled geologists. It has recently been  
25 documented that sulfate-reducing bacteria (SRB) are capable of catalyzing the  
26 formation of protodolomite, a previously proposed precursor of ordered sedimentary  
27 dolomite. However, the catalytic mechanism of SRB remains incompletely understood.  
28 This experimental study is aimed at probing the effect of capsule extracellular  
29 polymeric substances (capsule EPS) from SRB on the crystallization of protodolomite  
30 *in vivo*. The capsule EPS tested herein was isolated from a protodolomite-mediating  
31 SRB, *Desulfotomaculum ruminis*, and added into a solution wherein the degree of  
32 oversaturation was close to the growth medium of *D. ruminis* at stationary phase. The  
33 solid products were characterized with X-ray diffraction (XRD), Raman spectroscopy  
34 and, scanning and transmission electron microscopy (SEM and TEM). Our results  
35 indicated that aragonite emerged in the reactors without capsule EPS, while Ca-Mg  
36 carbonates (Mg-calcite and protodolomite) were produced in the systems amended with  
37 capsule EPS. The incorporation amount of Mg<sup>2+</sup> in Ca-Mg carbonates was enhanced  
38 with the increasing concentration of capsule EPS. The predominant occurrence of  
39 protodolomite was found in the reactor with 140 mg/L capsule EPS. These resulting  
40 protodolomites were spherical in shape, and composed of numerous nano-particles. The  
41 catalytic influence of capsule EPS on the precipitation of protodolomite might be  
42 attributed to their strong Mg<sup>2+</sup> binding capacity, potentially diminishing Mg-hydration,  
43 which is a potent inhibitor of protodolomite crystallization. The results of Fourier  
44 transformation infrared (FT-IR) spectra showed that Mg<sup>2+</sup> was bonded with carboxyl

45 and hydroxyl groups on capsule EPS. This inferred adsorption capacity of capsule EPS  
46 was also supported by new calculations of complexation chemistry between Mg-H<sub>2</sub>O  
47 complex and organic compounds present in capsule EPS.

48 **Keywords:** dolomite problem; protodolomite; capsule extracellular polymeric  
49 substances; sulfate-reducing bacteria; magnesium hydration

50

## 51 **1. Introduction**

52 The origin of sedimentary dolomite [CaMg(CO<sub>3</sub>)<sub>2</sub>] has been a persistent problem  
53 in the Earth sciences (Arvidson and Mackenzie, 1999; Warren, 2000; McKenzie and  
54 Vasconcelos, 2009). This so-called “dolomite problem” stems from the uneven  
55 distribution of dolomite abundance in the geological record and the difficulty in  
56 laboratory synthesis of dolomite at Earth surface temperatures (<60 °C) (Given and  
57 Wikinson, 1987; Land, 1998; Gregg et al., 2015). In general, modern seawater is  
58 oversaturated with respect to dolomite, however, this mineral is rarely found in recent  
59 marine sediments (Warren, 2000). In contrast, dolomite is a common constituent of  
60 Precambrian sedimentary rocks (Warren, 2000). It is now clear that the precipitation of  
61 dolomite is a kinetic-controlled process and the formation of stoichiometric dolomite  
62 proceeds stepwise through a series of metastable precursors (Rodriguez-Blanco et al.,  
63 2015; Kaczmarek and Thornton, 2017). Protodolomite, sometimes referred to as  
64 disordered dolomite or very high-Mg calcite, is a dolomite-like carbonate that displays  
65 near-dolomite stoichiometry, but with a disordered-cation arrangement, and it has been  
66 identified as a possible precursor phase in laboratory experiments (e.g., Graf and

67 Goldsmith, 1956; Malone et al., 1996; Rodriguez-Blanco et al., 2015; Kaczmarek and  
68 Thornton, 2017). According to previous experiments, the difficulty to precipitate low-  
69 temperature protodolomite is mainly attributed to the hydration effect of  $Mg^{2+}$   
70 (Lippmann, 1973; de Leeuw and Parker, 2001; Romanek et al., 2009; Shen et al., 2014,  
71 2015) and an intrinsic crystallization barrier impedes the subsequent transformation  
72 from protodolomite to a more stoichiometric and well-ordered dolomite (Xu et al.,  
73 2013).

74 Although Holocene dolomite is a rare precipitate in marine sediments, it is indeed  
75 discovered in some evaporitic environments (e.g., coastal lagoons, sabkhas and playa  
76 lakes) (e.g., Wright, 1999; van Lith et al., 2002; Bontognali et al., 2010; Deng et al.,  
77 2010; Meister et al., 2011; Brauchli et al., 2016; Petrash et al., 2017; McCormack et al.,  
78 2018; Liu et al., 2019a). Importantly, Holocene dolomites are normally Ca-rich and  
79 poorly ordered, and interpreted as being of primary or very early diagenetic origin  
80 (Petrash et al., 2017). Various hypotheses have been proposed to explain the genesis of  
81 Holocene dolomite. Among them, a microbial dolomite model has attracted much  
82 attention, arising from laboratory observations that some types of microorganism are  
83 effective in facilitating the precipitation of dolomite at ambient temperature  
84 (Vasconcelos et al., 1995; Sánchez-Román et al., 2008; McKenzie and Vasconcelos,  
85 2009; Petrash et al., 2017). It is worthwhile to note that these examples of microbially-  
86 induced dolomite were originally thought to be ordered dolomite, but recently have  
87 been alternatively interpreted as protodolomite because they lack evidence of cation  
88 ordering (Gregg et al., 2015). Nevertheless, as stated earlier, protodolomite is

89 considered as a precursor for some sedimentary dolomites and in this regard, the  
90 activity of microbes could be one possibility to account for the genesis of modern  
91 dolomites and some dolomicritic rocks (Petraş et al., 2017; Perri and Tucker, 2007;  
92 Fang and Xu, 2018; Huang et al., 2019).

93 Sulfate-reducing bacteria (SRB) are typical protodolomite-mediating microbes  
94 (Vasconcelos et al., 1995; van Lith et al., 2003; Bontognali et al., 2012). It has been  
95 proposed that the SRB facilitate the precipitation of protodolomite by increasing the  
96 saturation state of microenvironment around cells and by providing a template for  
97 protodolomite growth (van Lith et al., 2003; Bontognali et al., 2012). The soluble  
98 extracellular polymeric substances (i.e., slime EPS) derived from SRB have been  
99 demonstrated to be effective templating agents (e.g., Krause et al., 2012; Bontognali et  
100 al., 2014). These polymers are a complex mixture of protein, polysaccharide, uronic  
101 acid, lipid and nucleic acid (Beech and Cheung, 1995). As such, EPS are rich in various  
102 acid moieties (e.g., carboxylic, thiol, phosphate and hydroxyl functional groups)  
103 (Braissant et al., 2007), thus might be effective in binding the cations of  $Mg^{2+}$  and  $Ca^{2+}$ ,  
104 and potentially in diminishing the Mg-hydration effect (Bontognali et al., 2014).

105 In addition to slime EPS, there exists another kind of microbially-derived polymer  
106 called capsule or bound EPS (Beech and Cheung, 1995). Unlike slime EPS that are  
107 dissolved in solution, capsule EPS have a lower solubility and are located at cell surface  
108 as peripheral capsules (Beech and Cheung, 1995). In addition to their distinct physical  
109 states, it has been reported that these two types of EPS display some different chemical  
110 properties (e.g., polysaccharide/protein ratio) (Pan et al., 2010), which might result in

111 different influences on biomineralization. To date, however, few studies have examined  
112 the capacity of capsule EPS from SRB in protodolomite crystallization. Therefore, Ca-  
113 Mg carbonate nucleation experiments were performed to determine whether capsule  
114 EPS from protodolomite-mediating SRB facilitate the precipitation of protodolomite *in*  
115 *vivo*. The purpose of this study is to understand better the catalytic mechanism for the  
116 formation of low-temperature protodolomite by SRB.

117

## 118 **2. Materials and methods**

### 119 **2.1. SRB strain and culture medium**

120 *Desulfotomaculum ruminis* strain CGMCC 1.3470 has been demonstrated to be a  
121 protodolomite-mediating SRB (Deng et al., 2010), and was thus selected for our  
122 experiments. This strain was purchased from China General Microbiological Culture  
123 Collection Center (CGMCC). To avoid biomineralization which could influence  
124 biomass recovery and subsequent isolation of capsule EPS, *D. ruminis* was cultivated  
125 in an anaerobic Mg/Ca-free medium with salinity and sulfate concentration close to  
126 modern seawater. This medium consisted of (per liter) 4.5 g Na<sub>2</sub>SO<sub>4</sub>, 1 g NH<sub>4</sub>Cl, 0.5 g  
127 KH<sub>2</sub>PO<sub>4</sub>, 25 g NaCl, 2 g yeast extract, 20 mmol sodium lactate, 1 mL of trace elements  
128 solution (SL-10; Widdel et al., 1991), and 1 mL 0.1% resazurin (redox indicator). The  
129 pH of medium was adjusted to 7.5 by adding 0.1 M NaOH as needed. The medium was  
130 transferred to 100 mL serum bottles and further degassed by gushing ultra-pure N<sub>2</sub>. To  
131 better probe the changes in physico-chemical parameters upon microbial activity, the  
132 autoclaved serum bottles were inoculated with either live or dead cells of *D. ruminis* to

133 get the initial cell number of about  $5 \times 10^5$  cells/mL. The serum bottles were then  
134 incubated at 30 °C without agitation.

## 135 **2.2. Monitoring of cell growth and aqueous chemistry analysis during microbial** 136 **growth**

137 The cell density, solution pH and alkalinity were measured during incubation. The  
138 measurement of cell density was done by the acridine-orange direct counting (AODC)  
139 method. The pH was measured using a Denver UB-7 pH meter (Denver, USA).  
140 Alkalinity was determined by titration using 0.1 M HCl, with methyl orange as an  
141 indicator. The concentrations of  $\text{HCO}_3^-$  and  $\text{CO}_3^{2-}$  in the medium were calculated from  
142 measured pH and alkalinity using Visual MINTEQ 3.1 program (with “comp\_2008.vdb”  
143 as Component database). All measurements were performed in duplicate.

## 144 **2.3. Biomass collection and isolation of capsule EPS**

145 Once cell growth reached the stationary phase (as evidenced by AODC  
146 enumeration), cells of *D. ruminis* were harvested by centrifugation (7500×g, 10 min)  
147 in order to remove slime EPS and organic substrate. The obtained cell pellet was rinsed  
148 three times with 0.1 M  $\text{NaNO}_3$ . A portion of wet biomass was freeze dried and weighted  
149 to determine the biomass. Cell surface-bound capsule EPS (both loosely- and tightly-  
150 associated fractions included) were extracted from washed cells by using 10 mM  
151 ethylenediaminetetraacetate (EDTA) following a reported protocol (Liang et al., 2010).  
152 The capsule EPS suspension was filtered through 0.22  $\mu\text{m}$  filters to eliminate residual  
153 cell debris. The crude EPS was recovered from the suspension by using two volumes  
154 of cold ethanol (4 °C) and purified by dialysis (DCMW=3500 Da). Resulting EPS

155 extract was then concentrated prior to chemical quantification.

## 156 **2.4. Characterization of capsule EPS**

157 The surface charge of EPS (140 mg/L) was characterized by zeta potential titration  
158 at pH of 6, 7, 8, 9 and 10. These zeta potentials were quantified by a Malvern Zetasizer  
159 (Nano ZS, Malvern Instruments, UK). As protein, polysaccharide and uronic acid are  
160 the major components of EPS (Bazaka et al., 2011), their contents in our purified  
161 capsule EPS were determined by the methods described previously (François et al.,  
162 2012). Briefly, the protein content was analyzed using Bradford reagent (Sigma-Aldrich,  
163 USA) and bovine serum albumin as a standard. The content of polysaccharide was  
164 measured by the phenol-sulfuric acid method using glucose as a standard. The content  
165 of uronic acid was assayed using the hydroxydiphenyl method and glucuronic acid as a  
166 standard. The amino composition and monosaccharide of EPS were quantified with a  
167 high performance liquid chromatograph (HPLC; Agilent 1200, USA) coupled with a  
168 mass spectrometer (MS; Agilent 6460A, USA). Prior to the HPLC-MS analysis, EPS  
169 sample was acid hydrolyzed following the method of Qiu et al. (2017). Above  
170 determinations were performed in duplicate.

## 171 **2.5. Capsule EPS-assisted precipitation of Ca-Mg carbonates in a saturated** 172 **solution and analytical procedures**

### 173 **2.5.1. Abiotic synthesis of Ca-Mg carbonates in the presence of capsule EPS**

174 To test the templating effect of capsule EPS on Ca-Mg carbonate formation,  
175 abiotic carbonation experiments were carried out in a saturated solution, which were  
176 amended with different concentrations of capsule EPS (0, 70 and 140 mg/L). The

177 dosage of 140 mg/L was at the similar level to that determined at stationary phase (see  
178 later Section 3.1 for details). This precipitation solution contained the ions of  $\text{HCO}_3^-$   
179 and  $\text{CO}_3^{2-}$  at concentrations found in the culture medium at stationary phase.  
180 Furthermore, the starting concentrations of  $\text{Ca}^{2+}$  and  $\text{Mg}^{2+}$  in the precipitation solution  
181 were close to those of present seawater. In brief, the precipitation solution was prepared  
182 as follows: EPS powder was weighed and completely dissolved in a  
183  $\text{CaCl}_2/\text{MgCl}_2 \cdot 6\text{H}_2\text{O}$  solution (100 mL, 20 mM  $\text{Ca}^{2+}$  and 100 mM  $\text{Mg}^{2+}$ ) with vigorous  
184 stirring at 60 °C. After cooling to room temperature, this slime solution was added into  
185 the 50-mL serum bottles. The serum bottles were degassed with ultra-pure  $\text{N}_2$  and  
186 sealed with rubber stopper. An equal volume of pre-degassed bicarbonate/carbonate  
187 solution (117.2 mM  $\text{NaHCO}_3$  and 10.4 mM  $\text{Na}_2\text{CO}_3$ ) was immediately injected into the  
188 serum bottles to initiate carbonation. The resulting precipitation solutions were placed  
189 in an incubator at 30 °C without agitation for 15 days and all synthetic experiments  
190 reported were performed in duplicate.

### 191 **2.5.2. Chemical analyses and crystal characterization**

192 Solution pH during carbonate crystallization was measured at select time points.  
193 The concentrations of  $\text{Ca}^{2+}$  and  $\text{Mg}^{2+}$  were analyzed by inductively coupled plasma-  
194 optical emission spectrometry (ICP-OES, Thermofisher ICAP6300, USA), with an  
195 analytical precision of  $\pm 1\%$ . Total carbon (TC) and dissolved organic carbon (DOC) in  
196 the filtrate were detected by Shimadzu SCN analyzer (TOC-V, Shimadzu, Japan). The  
197 concentration of dissolved inorganic carbon (DIC) was calculated as the difference  
198 between TC and DOC. On the basis of these data, the saturation index (SI) with respect

199 to protodolomite was calculated by Visual MINTEQ (with “type6.vdb” for solids  
200 database).

201 At the end of experiments (day 15), the carbonate minerals were collected by  
202 centrifugation and rinsed five times with double distilled H<sub>2</sub>O, and then freeze-dried.  
203 The resulting solid samples were characterized by multiple approaches, including X-  
204 ray diffraction (XRD), Raman spectroscopy, scanning electron microscopy/energy  
205 dispersive spectroscopy (SEM-EDS), and transmission electron microscopy (TEM).

206 Specifically, the XRD measurements were conducted using a Scintag X1 X-ray  
207 powder diffractometer (Scintag Inc., USA) with Cu K $\alpha$  radiation (40 kV, 35 mA). The  
208 XRD data were smoothed and refined by the Rietveld method using a MDI JADE 6.0  
209 system. The MgCO<sub>3</sub> contents of Mg-calcites were calculated from the d-spacing of the  
210 (104) peak by using the calibration curve of Bischoff et al. (1983). For Raman  
211 spectroscopy, excitation was accomplished by a 20 mW 514.5 nm Ar<sup>+</sup> laser and detected  
212 by a RM-1000 laser Raman spectrometer (Renishaw, UK). The spectra were calibrated  
213 using the 520.5 cm<sup>-1</sup> line of silicon wafer. Samples were Pt-coated and examined under  
214 a SEM (SU8010, Hitachi, Japan) at 5-15 kV accelerated voltage. In addition, EDS (EX-  
215 350, Horiba, Japan) attached to the SEM was used to analyze the elemental composition  
216 of samples. TEM observations and selected area electron diffraction (SAED) were  
217 conducted on an FEI Talos F200X TEM with an accelerating voltage of 200 kV.

## 218 **2.6. Terminology of Ca-Mg carbonates**

219 In natural systems, the Ca<sup>2+</sup> sites in the lattice of calcite can be substituted by Mg<sup>2+</sup>  
220 ions, leading to the formation of various Ca-Mg carbonates that include Mg-calcite

221 (<36 mol% Mg<sup>2+</sup>; space group: *R3c*), protodolomite (with 36~55 mol% Mg<sup>2+</sup> and  
222 disordered cations; space group: *R3c*) and dolomite (space group: *R3*) (Zhang et al.,  
223 2015). These criteria were employed to categorize our solid products.

## 224 **2.7. Interaction of Mg<sup>2+</sup> with capsule EPS and complexation simulation**

225 As described before, the highly hydrated nature of Mg<sup>2+</sup> poses a challenge to the  
226 formation of Ca-Mg carbonates (e.g., protodolomite). A metal-chelation mechanism  
227 has been proposed to interpret the role of slime EPS in dehydration of Mg (Bontognali  
228 et al., 2014). In order to assess which functional groups of capsule EPS are responsible  
229 for Mg complexation, a Mg-adsorption experiment was conducted. This was performed  
230 in a 50 mL centrifuge tube with 40 mL of capsule EPS-containing solution (150 mg/L),  
231 which was allowed to interact with 50 mM MgCl<sub>2</sub>. The tube was shaken at 30 °C and  
232 160 rpm for 6 h. EPS sample was recovered by a freeze-drying process. The Fourier  
233 transformation infrared (FT-IR) spectra of capsule EPS before and after Mg<sup>2+</sup>  
234 adsorption were recorded on a Perkin-Elmer FT-IR spectrometer (Model 2000; Perkin-  
235 Elmer co., USA).

236 Lastly, complexation chemistry between Mg-H<sub>2</sub>O complex and organic  
237 compounds from capsule EPS was further modeled using density functional theory  
238 (DFT) calculations. Instead of the high-molecular weight and heterogeneous EPS,  
239 typical monomeric organic compounds, which compose capsule EPS of *D. ruminis*,  
240 were selected as representatives for our stimulations. The geometry optimizations were  
241 carried out by the M06-2X functional. The standard 6-31G(d, p) basis sets were  
242 employed for the H, C, O and Mg atoms for the electronic structure calculations. All

243 calculations were performed using the Gaussian 09 software package.

244

### 245 **3. Results**

#### 246 **3.1. Changes in cell density and aqueous chemistry during microbial growth**

247 No growth was observed in the systems with dead cells of *D. ruminis* (Fig. 1A).  
248 By contrast, the cell density showed a rapid rise after inoculation with live cells. It  
249 increased from ca.  $5 \times 10^5$  cells/mL to  $2 \times 10^8$  cells/mL for the first 5 d followed by a  
250 stationary phase. The solution pH exhibited an expression pattern similar to cell density  
251 (Fig. 1B). In brief, the pH changes in dead cell inoculum treatments were negligible,  
252 while the pH in the reactors with active cells increased to 9.02 by the end of incubation  
253 (day 10). As a consequence of microbial sulfate reduction, the solution alkalinity in the  
254 treatments with live cells was sharply elevated from near 0 (at day 0) to 63.96 mM by  
255 day 10 (Fig. 1C). Based on the measurements of solution pH and alkalinity, the  
256 concentrations of  $\text{CO}_3^{2-}$  and  $\text{HCO}_3^-$  on day 10 were calculated as 5.2 and 58.6 mM,  
257 respectively (Fig. 1D). At the end of incubation, the dry weight was 578.4 mg/L for  
258 biomass and 140.3 mg/L for capsule EPS, respectively (Fig. 1D).

#### 259 **3.2. The properties of capsule EPS from *D. ruminis***

260 As shown in Fig. 2A, capsule EPS of *D. ruminis* were negatively charged, as  
261 evidenced by the fact that the value of zeta potential was in the range from -74.5 to -  
262 105.9 mV at different pHs. The major fraction of the capsule EPS sample was  
263 composed of protein, polysaccharide and uronic acid (Fig. 2B). Specifically, the content  
264 of protein was 397.8 mg/g, higher than that of polysaccharide (227.1 mg/g) and uronic

265 acid (24.9 mg/g). The amino acids derived from EPS-associated protein were further  
266 analyzed. The results showed that various acidic, basic and neutral amino acids were  
267 detected (Fig. 2C). Among them, acidic amino acids such as glutamic and aspartic acid  
268 were most abundant. The molar ratio of acidic to basic amino acids was 2.84. Moreover,  
269 our results also indicated that the saccharide fraction of capsule EPS mainly consisted  
270 of mannose (58.2%), glucose (20.4%), xylose (15.9%) and fructose (5.5%) (Fig. 2D).

### 271 **3.3. Evolution of aqueous chemistry upon carbonation without and with capsule** 272 **EPS**

273 When the mixture solution of  $\text{NaHCO}_3$  and  $\text{Na}_2\text{CO}_3$  was added into the Ca/Mg  
274 solution, gel-like precipitates immediately occurred. As a result of carbonation, the  
275 aqueous chemistry was dynamically changed and showed differences in the reactors  
276 without or with capsule EPS (Fig. 3).

277 The pH in all reactors generally decreased over time and these decreases were  
278 significantly related to the increased dosage of capsule EPS (Fig. 3A). Specifically, the  
279 pH in reactors without EPS (0 mg/L) declined from 9.01 to 8.71 at the end of  
280 experiments (day 15). The pH in reactors amended with 70 mg/L capsule EPS  
281 decreased to 8.68, and the pH in reactors with 140 mg/L capsule EPS decreased to 8.64.

282 The concentrations of  $\text{Ca}^{2+}$  dropped sharply at a similar rate for each treatment  
283 (Fig. 3B). After carbonation, most of the  $\text{Ca}^{2+}$  ions were removed from solution and the  
284 remaining concentrations of  $\text{Ca}^{2+}$  were only ca. 1.04 mM. In contrast, the decrease in  
285 the concentration of  $\text{Mg}^{2+}$  exhibited large differences when different dosages of capsule  
286 EPS were used (Fig. 3C). The concentration of  $\text{Mg}^{2+}$  was nearly kept constant in the

287 absence of EPS, while a decline was observed in the reactors with capsule EPS, which  
288 became more obvious under higher concentration of capsule EPS.

289 As shown in Fig. 3D, the changes of DIC displayed trends similar to those of pH  
290 (Fig. 3A), indicating that the depletion of  $\text{HCO}_3^-$  and  $\text{CO}_3^{2-}$  primarily accounted for the  
291 detected pH decline. The saturation index with respect to protodolomite was further  
292 calculated. In general, the solution in each reactor was oversaturated during carbonation  
293 experiments (Fig. 3E). The concentration of precipitated Mg (depletion of  $\text{Mg}^{2+}$ ) was  
294 linearly correlated with that of precipitated Ca (Fig. 3F). It is important to note that the  
295 precipitated Mg was nearly equal to the precipitated Ca in the systems with 140 mg/L  
296 capsule EPS.

### 297 **3.4. Characterization of the produced carbonates**

298 The XRD results revealed that the crystals formed in the absence of EPS were  
299 exclusively aragonite (Fig. 4A). When capsule EPS were introduced into the precipitate  
300 solution, the solid products were significantly changed (Figs. 4B and 5). Specifically,  
301 Mg-calcite was the dominant phase in the systems with 70 mg/L capsule EPS. Its  
302 highest-intensity (104) peak centered around  $30.209^\circ 2\theta$  (Cu  $K\alpha$ ), corresponding to a  
303 d-spacing value of 2.956 Å (Fig. 4B). This value revealed that the obtained Mg-calcite  
304 had an average  $\text{MgCO}_3$  content of 28.2 mol% (Bischoff et al., 1983). SEM results  
305 showed that these Mg-calcites were micron-sized crystals with a spherical morphology  
306 (Fig. 4B).

307 Once the concentration of capsule EPS increased up to 140 mg/L (close to the  
308 capsule EPS yield at stationary phase), the d(104) of newly-formed Ca-Mg carbonate

309 shifted to 2.914 Å (Fig. 5A), corresponding to 43.5 mol% MgCO<sub>3</sub> in its structure  
310 (Bischoff et al., 1983). This value approached that of stoichiometric dolomite (50 mol%  
311 of MgCO<sub>3</sub>). Given the fact that no visible ordering peaks [e.g., (015) and (021)] could  
312 be found in the XRD pattern, this dolomite-like mineral thus can be identified as  
313 protodolomite. The Raman spectrum in the 100-1200 cm<sup>-1</sup> region indicated that our  
314 protodolomite displayed four intense bands at 172, 297, 724 and 1095 cm<sup>-1</sup>, respectively,  
315 much closer to those of dolomites reported elsewhere (e.g., Perrin et al., 2016). SEM  
316 observations showed that protodolomite crystals were about 6-8 μm in size and had  
317 spherical shapes (Fig. 5C). The EDS spot data confirmed that protodolomite contained  
318 approximately similar contents of Mg and Ca (Kα line). Interestingly, a magnified view  
319 showed that micron-sized protodolomite was composed of densely packed nano-grains  
320 (Fig. 5D). Elemental mapping by EDS revealed that Ca and Mg in protodolomite were  
321 homogeneously distributed (Fig. 5E). The microstructure of resulting protodolomite was  
322 investigated by TEM. The fringe spacing was measured to be 2.91 Å, corresponding to  
323 the (104) plane of protodolomite (Fig. 5F). In agreement with XRD data, the disordered  
324 structure of protodolomite was also confirmed by its SAED pattern, which lacked  
325 superlattice reflections [e.g., (015), and (021)] (Fig. 5F).

### 326 **3.5. Magnesium binding mechanism onto capsule EPS revealed by FT-IR and** 327 **DFT calculations**

328 FT-IR spectra of pristine and Mg-adsorbed capsule EPS are shown in Fig. 6. For  
329 pristine sample, the main IR absorption peaks were observed at 1075, 1239, 1399, 1540  
330 and 1651 cm<sup>-1</sup>, which are normally assigned to –OH group of polysaccharide,

331 phosphate group of nucleic acid, and three functional groups from amides of protein  
332 (i.e.,  $-\text{COO}^-$ ,  $\text{N-H}$ ,  $\text{C=O}$ ), respectively (Omoike and Chorover, 2004). These bands of  
333 functional group were also found in the Mg-adsorbed capsule EPS. However, changes  
334 in the position of some peaks occurred: the peaks of hydroxyl group ( $-\text{OH}$ ) and  
335 carboxyl group ( $-\text{COO}^-$ ) shifted to  $1069\text{ cm}^{-1}$  and to  $1388\text{ cm}^{-1}$ , respectively. Given  
336 these results, we suggest that phosphate and saccharide-derived hydroxyl groups and  
337 carboxyl sites in amino acid might be responsible for the binding of Mg onto capsule  
338 EPS.

339 The binding sites of Mg and capsule EPS (glutamic acid and mannose as  
340 representatives) were further explored by the DFT calculation. The calculated  
341 interaction energy between  $\text{Mg}^{2+}$  and water molecules is  $-62.2\text{ kcal/mol}$ . When Mg-  
342  $\text{H}_2\text{O}$  complex [i.e.,  $\text{Mg}(\text{H}_2\text{O})_6^{2+}$ ] interacts with organic compounds, the adsorption  
343 energy was  $-251.2\text{ kcal/mol}$  for glutamic acid and  $-242.9\text{ kcal/mol}$  for mannose,  
344 respectively. These data indicate that the binding of Mg- $\text{H}_2\text{O}$  complexes to the hydroxyl  
345 and carboxyl groups on capsule EPS and accompanying water ejection are energy-  
346 favored processes. Figure 7 provides the optimized structures of  $\text{Mg}^{2+}$  interaction with  
347 water molecules, glutamic acid and mannose. The bond length of Mg-O in  $\text{Mg}(\text{H}_2\text{O})_6^{2+}$   
348 is  $2.060\text{ \AA}$  and thus longer than the Mg-O bond between  $\text{Mg}^{2+}$  and glutamic acid and  
349 mannose, which are  $2.003\text{ \AA}$  and  $1.959\text{ \AA}$ , respectively (Fig.7), further revealing the  
350 strong binding of Mg with the hydroxyl and carboxyl groups.

351

#### 352 4. Discussion

#### 353 **4.1. Catalytic role of capsule EPS in the crystallization of Ca-Mg carbonates**

354 Calcite is an effective host for  $Mg^{2+}$  (Loste et al., 2003; Sommerdijk and de With,  
355 2008). However, aragonite rather than calcite is the expected kinetically-favored  
356 product when the Mg/Ca molar ratio of saturated solution exceeds 4.0 (Morse et al.,  
357 1997). Such phenomenon is generally thought to be caused by the Mg-hydration effect  
358 (Romanek et al., 2009; Lenders et al., 2012; Zhang et al., 2012a, b; Shen et al., 2014,  
359 2015). Similarly to  $Ca^{2+}$  ions,  $Mg^{2+}$  ions are primarily bound to water molecules,  
360 thereby generating Mg-H<sub>2</sub>O complexes [i.e.,  $Mg(H_2O)_6^{2+}$ ] (Lippmann, 1973; Romanek  
361 et al., 2009; Hamm et al., 2010). However,  $Mg^{2+}$  has much lower water exchange rate  
362 than does  $Ca^{2+}$  (Pavlov et al., 1998). Specifically, the lifetime of water molecules  
363 around  $Ca^{2+}$  is around 18 ps (Jiao et al., 2006). In contrast, the lifetime of Mg-H<sub>2</sub>O  
364 complex is as long as 600 ps (Jiao et al., 2006). Additionally, it has been reported that  
365 the dehydration enthalpy ( $\Delta H$ ) is 351.8 kcal/mol for  $Mg(H_2O)_6^{2+}$  under standard  
366 conditions (298 K, 1 atm), which is significantly larger than that for  $Ca(H_2O)_6^{2+}$  (264.3  
367 kcal/mol) (Katz et al., 1996). These results suggest that there is a stronger interaction  
368 between  $Mg^{2+}$  and water molecules than  $Ca^{2+}$  (Romanek et al., 2009).

369 Once massive stable Mg-H<sub>2</sub>O complexes enter into the growing calcite, the  
370 hydration spheres of  $Mg^{2+}$  could block the binding of carbonate to Ca or Mg ions, thus  
371 poisoning the calcitic structure (Loste et al., 2003). However, the denser aragonite  
372 structure incorporates far fewer  $Mg^{2+}$  ions, and therefore precipitation of aragonite is  
373 not inhibited in Mg-bearing solutions (Zhang et al., 2012a, b). For this reason, it is no  
374 surprise that aragonite dominates over Ca-Mg carbonates (e.g., Mg-calcite and

375 protodolomite) in our EPS-free reactors, in which the Mg/Ca molar ratio is around 5.0.

376 In the present study, however, the precipitation of Mg-calcite and protodolomite  
377 could take place in the presence of capsule EPS from *D. ruminis*, thereby revealing that  
378 SRB-derived capsule EPS might be as effective as their slime EPS in dewatering of  
379 Mg-H<sub>2</sub>O complexes (Krause et al., 2012; Bontognali et al., 2014). According to  
380 previous studies, the dehydration capacity of Mg-H<sub>2</sub>O complexes by slime EPS is  
381 substantially attributed to the carboxyl moiety of their protein fraction (e.g., Kenward  
382 et al., 2013; Roberts et al., 2013). It has been proposed that carboxyl groups within  
383 slime EPS matrix can bind Mg-H<sub>2</sub>O complexes via electrostatic attraction (Kenward et  
384 al., 2013). Our DFT results calculations indicated that Mg-H<sub>2</sub>O complexes binding to  
385 capsule EPS are also thermodynamically favorable. Upon binding to carboxyl groups,  
386 one of the water molecules in Mg-H<sub>2</sub>O complexes would be replaced by a carboxyl  
387 group and Mg-carboxyl clusters could be produced  $[\text{Mg}(\text{H}_2\text{O})_6^{2+} + \text{R-COO}^- \rightarrow$   
388  $\text{Mg}(\text{H}_2\text{O})_5(\text{R-COO})^+ + \text{H}_2\text{O}]$  (Roberts et al., 2013). Compared to Mg-H<sub>2</sub>O complex,  
389 Mg-carboxyl cluster requires lower energy for carbonation and the subsequent  
390 attachment of Ca<sup>2+</sup> (Romanek et al., 2009; Roberts et al., 2013; Qiu et al., 2017). As  
391 such, a Ca-Mg carbonate layer on EPS could be created with the aid of EPS and it  
392 subsequently acts as a nucleus for crystal growth if the super-saturation is maintained  
393 (Roberts et al., 2013).

394 Polysaccharide is also an important constituent of capsule EPS from *D. ruminis*  
395 and it is rich in hydroxyl groups. Our experiments showed that these hydroxyl groups  
396 might be an overlooked facilitator for accelerating Mg dehydration and subsequent

397 crystal nucleation. Similarly to carboxyl group, hydroxyl moiety is also negatively  
398 charged. It can thus be presumed that EPS-bound hydroxyl groups promote Mg  
399 dehydration in a similar fashion to carboxyl groups described above, i.e., through a  
400 metal-chelation mechanism. Interestingly, a similar observation regarding OH-induced  
401 Mg-dehydration was made in our previous work, which demonstrated that mineral  
402 surface-bound hydroxyl attributed to the positive role of clays in triggering the  
403 production of protodolomite from oversaturated solution (Liu et al., 2019b).  
404 Furthermore, the possible existence of other catalytic functional groups besides  
405 carboxyl and hydroxyl should be examined in future studies.

406       Compared to slime EPS, capsule EPS function as an outer envelope around cell  
407 surface. Therefore, microbial cells with capsule EPS can exhibit a solid-like catalyst for  
408 the crystallization of Ca-Mg carbonates. It has also been proposed that the interfacial  
409 free energy between two solid phases (e.g., Ca-Mg carbonates and EPS-enveloped cells)  
410 is smaller than that between the solid and the solution (e.g., Ca-Mg carbonates and  
411 slime EPS) (Stumm and Morgan, 1996). As such, capsule EPS may be more effective  
412 in triggering the precipitation of Ca-Mg carbonates than slime EPS. Furthermore, the  
413 catalytic effect of capsule EPS shown herein can interpret previous findings on the  
414 precipitation of Ca-Mg carbonates from oversaturated solutions induced by inactive  
415 microbial cells (Kenward et al., 2013; Zhang et al., 2015), and on the encrusted cells by  
416 carbonate minerals in some cases (e.g., Aloisi et al., 2006).

#### 417 **4.2. Mg-calcite vs. protodolomite**

418       In our laboratory experiments, Mg-calcite formed in the presence of lower

419 concentration of capsule EPS (70 mg/L), showing the occurrence of non-simultaneous  
420 uptakes of Ca and Mg into Ca-Mg carbonate. In fact, similar findings have also been  
421 previously reported using carboxylic acids (Han et al., 2013), polysaccharides (Zhang  
422 et al., 2012a), peptides (Stephenson et al., 2008) and capsule EPS that were isolated  
423 from an anaerobic mixed culture (Zhang et al., 2015). The above phenomenon can be  
424 explained by the different tendencies of organic molecules for Mg and Ca adsorption.  
425 It has been well documented that carboxyl-rich compounds (e.g., EPS) bind more  $\text{Ca}^{2+}$   
426 than  $\text{Mg}^{2+}$ , principally due to more energy required to dissociate the hydration shell of  
427  $\text{Mg}^{2+}$  (Wang et al., 2009; Krause et al., 2012). As such, it is reasonable to assume that  
428 the Ca-Mg carbonate layer with a high content of  $\text{Ca}^{2+}$  (i.e., Mg-calcite) preferentially  
429 forms within EPS matrix. Once such Mg-calcite layer is generated, as a  
430 thermodynamically-favorable process, its epitaxial growth rather than spontaneous  
431 nucleation of other minerals would take place (Rodriguez-Navarro et al., 2012).

432 However, protodolomite with nearly equal molar contents of Ca and Mg was  
433 produced when a higher dosage of capsule EPS (140 mg/L) was used. Actually, this  
434 concentration-dependent catalytic fashion has also been observed in previous studies  
435 (Zhang et al., 2012a, 2015). Undoubtedly, more binding sites can be provided in the  
436 reactors with high concentration of capsule EPS. In spite of the competitive binding of  
437  $\text{Ca}^{2+}$  and  $\text{Mg}^{2+}$  onto capsule EPS, the existence of sufficient binding sites and high  
438 Mg/Ca ratio might allow further accumulation of Mg on EPS after that the  
439 complexation with  $\text{Ca}^{2+}$  leveled off. In doing so, the nucleation and growth of  
440 protodolomite should be possible.

441 Our microscopy results revealed that both Mg-calcite and protodolomite had  
442 spherical shapes. This notable crystal feature has been observed in microbially-induced  
443 carbonates produced in laboratory (e.g., Aloisi et al., 2006; Bontognali et al., 2008;  
444 Sánchez-Román et al., 2008, 2011; Sánchez-Navas et al., 2009; Krause et al., 2018) and  
445 also been encountered in rock records (e.g., Perri and Tucker, 2007; You et al., 2013).  
446 However, morphology should be not suitable as a single criterion differentiating  
447 microbially-induced carbonates from abiotic counterparts, because similar crystal  
448 shapes have also been found in abiotically-synthesized Ca-Mg carbonates (Rodríguez-  
449 Blanco et al., 2015; Liu et al., 2019a, b). Actually, spherulites are relatively common  
450 crystalline structure observed in polymer systems, especially at high levels of  
451 supersaturation (Rodríguez-Blanco et al., 2015). High supersaturation can act as a  
452 driving force for the formation of spherical polycrystalline aggregation via a growth  
453 front nucleation mechanism (Gránásy et al., 2005; Rodríguez-Blanco et al., 2015).  
454 Given the presence of capsule EPS and super-saturated solution ( $SI_{\text{protodolomite}} > 4$ , Fig.  
455 3E) used in this study, it is expected that the crystallization of Mg-calcite and  
456 protodolomite proceeded via spherulitic growth, as shown in Fig. 5.

### 457 **4.3. Formation mechanisms of protodolomite by SRB**

458 Sulfate-reducing bacteria are thought to be a critical component of the “alkalinity  
459 engine” in sedimentary settings (Gallagher et al., 2012). It has been suggested that the  
460 microbial sulfate reduction is responsible for more than 50% of organic matter  
461 mineralization within microbial mats (Visscher et al., 1998). During the decomposition  
462 of organic matter, SRB activity normally increases both the pH and DIC concentration

463 in porewaters of sediments and microbial mats, thereby increasing protodolomite  
464 saturation (Vasconcelos et al., 1995; Bontognali et al., 2014). Additionally, their  
465 exudates (e.g., slime EPS) and by-product H<sub>2</sub>S from sulfate reduction have been shown  
466 to effectively weaken the hydration shell of Mg<sup>2+</sup>, which is a prerequisite for the  
467 precipitation of protodolomite from saturated solutions (Krause et al., 2012; Zhang et  
468 al., 2012b; Bontognali et al., 2014). In this study, we also demonstrated that capsule  
469 EPS of SRB could aid in the formation of protodolomite, perhaps via desolvation of the  
470 hydrated Mg<sup>2+</sup> ions. Our results, together with others, reveal that multiple triggers are  
471 involved in SRB-mediated protodolomite formation.

#### 472 **4.4. Geological implications**

473 Despite the globally cosmopolitan nature of SRB, their abundance varies with  
474 habitat type (Rabus et al., 2013). Compared to other environments, hypersaline aquatic  
475 environments normally have higher primary productivity and higher concentration of  
476 sulfate ions (Oren, 2012). As such, high sulfate-reducing rates and high numbers of  
477 SRB are measured in inland lakes, coastal lagoons and other evaporitic settings (e.g.,  
478 Brandt et al., 2001; Wright and Wacey, 2005; Kjeldsen et al., 2007). For instance, anoxic  
479 sediments of the Great Salt Lake harbor large populations of SRB in the range from  
480  $2.2 \times 10^7$  to  $6.7 \times 10^8$  cells/mL (Brandt et al., 2001).

481 Our study demonstrated that the precipitation of protodolomite seemed only to  
482 proceed with the aid of high concentration of capsule EPS. This dosage was close to  
483 the capsule EPS yield produced by SRB with a cell number of  $\sim 2 \times 10^8$  cells/mL. These  
484 results likely explain why modern dolomites are frequently discovered in evaporitic

485 environments, because there exist several trigger factors that include the prevalence of  
486 microbial sulfate reduction and high amounts of EPS (both capsule and slime EPS  
487 included) as well as high salinity. It has been documented that elevated solution salinity  
488 not only enhances the microbial EPS production (Qiu et al., 2012), but also increases  
489 the density of carboxyl groups on microbial cell surface (Voegerl, 2014; Qiu et al.,  
490 2017). Indeed, Wacey and co-worker reported that the dolomite-forming lakes in  
491 Coorong region (Australia) had much larger numbers of SRB than other neighbouring  
492 but non-dolomitic lakes (Wacey et al., 2007).

493 Our microscopic data indicated that the resulting protodolomites appeared to be  
494 mesocrystal, which are built up from nano-sized grains (Cölfen and Antonietti, 2005).  
495 It is generally thought that mesocrystals are quite unstable because of their high lattice  
496 energy (Cölfen and Antonietti, 2005). Therefore, as a metastable intermediate,  
497 protodolomite occurring in sediments tends to convert into more stoichiometric  
498 dolomite when subjected to increasing temperatures during burial diagenesis (Malone  
499 et al., 1996; Rodriguez-Blanco et al., 2015). In this regard, the microbial EPS-catalyzed  
500 dolomite precipitation offers one possibility for interpreting the origin of sedimentary  
501 dolomites in the Precambrian record.

502

## 503 **5. Conclusions**

504 We demonstrated that capsule EPS from *D. ruminis* acted in a concentration  
505 dependent manner to facilitate the loading of Mg<sup>2+</sup> during Ca-Mg carbonate growth. In  
506 the absence of capsule EPS, aragonite was precipitated from a solution at a similar

507 saturation level to the growth medium for *D. ruminis* at stationary phase. However, Mg-  
508 calcite and dolomite-like material occurred in the reactors with 70 mg/L and 140 mg/L  
509 capsule EPS, respectively. The cation arrangement in dolomite-like material was  
510 disordered as confirmed by the results of XRD and TEM, indicating the formation of  
511 protodolomite. The protodolomite crystals displayed spherical shapes and were a few  
512 micrometers in size. The positive role of capsule EPS in dewatering Mg-H<sub>2</sub>O  
513 complexes might account for their catalytic influence on the crystallization of  
514 protodolomite. The capacity of capsule EPS for diminishing Mg hydration was mainly  
515 attributed to the binding of Mg<sup>2+</sup> by carboxyl and hydroxyl groups on EPS.

516

## 517 **Acknowledgments**

518 This research is financially supported by grants from the National Natural Science  
519 Foundation of China (Nos. 41772362, 41572323 and 41502317), the Strategic Priority  
520 Research Program of Chinese Academy of Sciences (No. XDB26000000), the 111  
521 Project (No. B08030), and the Fundamental Research Funds for the Central  
522 Universities, China University of Geosciences (Wuhan) (CUGCJ1703). The authors are  
523 grateful to Prof. Rolf S. Arvidson and an anonymous reviewer for thoughtful comments  
524 on the manuscript.

525

## 526 **References**

527 Aloisi, G., Gloter, A., Krüger, M., Wallmann, K., Guyot, F., Zuddas, P., 2006.

528 Nucleation of calcium carbonate on bacterial nanoglobules. *Geology* 34(12),

529 1017-1020.

530 Arvidson, R.S., Mackenzie, F.T., 1999. The dolomite problem: control of precipitation  
531 kinetics by temperature and saturation state. *Am. J. Sci.* 299, 257-288.

532 Bazaka, K., Crawford, R.J., Nazarenko, E.L., Ivanova, E.P., 2011. Bacterial  
533 extracellular polysaccharides. *Adv. Exp. Med. Biol.* 715, 213-226.

534 Beech, I.B., Cheung, C.W.S., 1995. Interactions of exopolymers produced by sulfate-  
535 reducing bacteria with metal ions. *Int. Biodeterior. Biodegrad.* 35, 59-72.

536 Bischoff, W.D., Bishop, F.C., Mackenzie, F.T., 1983. Biogenically produced magnesian  
537 calcite: inhomogeneities in chemical and physical properties; comparison with  
538 synthetic phases. *Am. Mineral.* 68, 1183-1188.

539 Bontognali, T.R.R., Vasconcelos, C., Warthmann, R.J., Dupraz, C., Bernasconi, S.M.,  
540 McKenzie, J.A., 2008. Microbes produce nanobacteria-like structures, avoiding  
541 cell entombment. *Geology* 36, 663-666.

542 Bontognali, T.R.R., Vasconcelos, C., Warthmann, R.J., Bernasconi, S.M., Dupraz, C.,  
543 Stohmenger, C.J., McKenzie, J.A., 2010. Dolomite formation within microbial  
544 mats in the coastal sabkha of Abu Dhabi (United Arab Emirates).  
545 *Sedimentology* 57, 824-844.

546 Bontognali, T.R.R., Vasconcelos, C., Warthmann, R.J., Lundberg, R., McKenzie, J.A.,  
547 2012. Dolomite-mediating bacterium isolated from the sabkha of Abu Dhabi  
548 (UAE). *Terra Nova* 24, 248-254.

549 Bontognali, T.R.R., McKenzie, J.A., Warthmann, R.J., Vasconcelos, C., 2014.  
550 Microbially influenced formation of Mg-calcite and Ca-dolomite in the

551 presence of exopolymeric substances produced by sulphate-reducing bacteria.  
552 Terra Nova 26, 72-77.

553 Braissant, O., Decho, A.W., Dupraz, C., Glunk, C., Przekop, K.M., Visscher, P.T., 2007.  
554 Exopolymeric substances of sulfate-reducing bacteria: Interactions with  
555 calcium at alkaline pH and implication for formation of carbonate minerals.  
556 Geobiology 5, 401-411.

557 Brandt, K.K., Vester, F., Jensen, A.N., Ingvorsen, K., 2001. Sulfate reduction dynamics  
558 and enumeration of sulfate-reducing bacteria in hypersaline sediments of the  
559 Great Salt Lake (Utah, USA). Microb. Ecol. 41, 1-11.

560 Brauchli, M., McKezie, J.A., Strohmenger, C.J., Sadooni, F., Vasconcelos, C.,  
561 Bontognali, T.R.R., 2016. The importance of microbial mats for dolomite  
562 formation in the Dohat Faishakh sabkha, Qatar. Carbonate. Evaporite. 31, 339-  
563 345.

564 Cölfen, H., Antonietti, M., 2005. Mesocrystals: Inorganic superstructures made by  
565 highly parallel crystallization and controlled alignment. Angew. Chem. Int. Ed.  
566 44, 5576-5591.

567 de Leeuw, N.H., Parker, S.C., 2001. Surface-water interactions in the dolomite problem.  
568 Phys. Chem. Chem. Phys. 3(15), 3217-3221.

569 Deng, S., Dong, H., Lv, G., Jiang, H., Yu, B., Bishop, M.E., 2010. Microbial dolomite  
570 precipitation using sulfate reducing and halophilic bacteria: Results from  
571 Qinghai Lake, Tibetan Plateau, NW China. Chem. Geol. 278, 151-159.

572 Fang, Y., Xu, H., 2018. Study of an Ordovician carbonate with alternating dolomite-

573 calcite laminations and its implication for catalytic effects of microbes on the  
574 formation of sedimentary dolomite. *J. Sed. Res.* 88, 679-695.

575 François, F., Lombard, C., Guigner, J., Soreau, P., Brian-Jaisson, F., Martino, G.,  
576 Vandervennet, M., Garcia, D., Molinier, A., Pignol, D., Peduzzi, J., Zirah, S.,  
577 Rebuffat, S., 2012. Isolation and characterization of environmental bacteria  
578 capable of extracellular biosorption of mercury. *Appl. Environ. Microbiol.* 78(4),  
579 1097-1106.

580 Gallagher, K.L., Kading, T.J., Braissant, O., Duparaz, C., Visscher, P.T., 2012. Inside  
581 the alkalinity engine: the role of electron donors in the organomineralization  
582 potential of sulfate-reducing bacteria. *Geobiology* 10, 518-530.

583 Given, R.K., Wilkinson, B.H., 1987. Dolomite abundance and stratigraphic age:  
584 constraints on rates and mechanisms of Phanerozoic dolostone formation:  
585 Perspectives. *J. Sediment. Petrol.* 57(6), 1068-1078.

586 Graf, D.L., Goldsmith, J.R., 1956. Some hydrothermal syntheses of dolomite and  
587 protodolomite. *J. Geol.* 64, 173-186.

588 Gránásy, L., Pusztai, T., Tegze, G., Warren, J.A., Douglas, J.F., 2005. Growth and form  
589 of spherulites. *Phys. Rev. E* 72, 011605.

590 Gregg, J.M., Bish, D.L., Kaczmarek, S.E., Machel, H.G., 2015. Mineralogy, nucleation  
591 and growth of dolomite in the laboratory and sedimentary environment: a review.  
592 *Sedimentology* 62, 1749-1769.

593 Hamm, L.M., Wallace, A.F., Dove, P.M., 2010. Molecular dynamics of ion hydration in  
594 the presence of small carboxylated molecules and implications for calcification.

595 J. Phys. Chem. B 114, 10488-10495.

596 Huang, Y., Yao, Q., Li, H., Wang, F., Zhou, G., Fu, S., 2019. Aerobically incubated  
597 bacterial biomass-promoted formation of disordered dolomite and implication  
598 for dolomite formation. Chem. Geol. 523, 19-30.

599 Jiao, D., King, C., Grossfield, A., Darden, T.A., Ren, P., 2006. Simulation of Ca<sup>2+</sup> and  
600 Mg<sup>2+</sup> solvation using polarizable atomic multipole potential. J. Phys. Chem. B  
601 110, 18553-18559.

602 Kaczmarek, S.E., Thornton, B.P., 2017. The effect of temperature on stoichiometry,  
603 cation ordering, and reaction rate in high-temperature dolomitization  
604 experiments. Chem. Geol. 468, 32-41.

605 Katz, A.K., Glusker, J.P., Beebe, S.A., Bock, C.W., 1996. Calcium ion coordination: a  
606 comparison with that of beryllium, magnesium, and zinc. J. Am. Chem. Soc.  
607 118, 5752-5763.

608 Kenward, P.A., Fowle, D.A., Goldstein, R.H., Ueshima, M., González, L.A., Roberts,  
609 J.A., 2013. Ordered low-temperature dolomite mediated by carboxyl-group  
610 density of microbial cell walls. AAPG Bull. 97, 2113-2125.

611 Kjeldsen, K.U., Loy, A., Jakobsen, T.F., Thomsen, T.R., Wagner, M., Ingvorsen, K.,  
612 2007. Diversity of sulfate-reducing bacteria from an extreme hypersaline  
613 sediment, Great Salt Lake (Utah). FEMS Microbiol. Ecol. 60, 287-298.

614 Krause, S., Liebetrau, V., Gorb, S., Sánchez-Román, M., McKenzie, J.A., Treude, T.,  
615 2012. Microbial nucleation of Mg-rich dolomite in exopolymeric substances  
616 under anoxic modern seawater salinity: new insight into an old enigma. Geology

617 40, 587-590.

618 Krause, S., Liebetrau, V., Löscher, C.R., Böhm, F., Gorb, S., Eisenhauser, A., Treude,  
619 T., 2018. Marine ammonification and carbonic anhydrase activity induce rapid  
620 calcium carbonate precipitation. *Geochim. Cosmochim. Acta* 243, 116-132.

621 Land, L.S., 1998. Failure to precipitate dolomite at 25°C from dilute solution despite  
622 1000-fold oversaturation after 32 years. *Aquat. Geochem.* 4, 361-368.

623 Lenders, J.J.M., Dey, A., Bomans, P.H.H., Spielmann, J., Hendrix, M.M.R.M., de With,  
624 G., Meldrum, F.C., Harder, S., Sommerdijk, N.A.J.M., 2012. High-magnesian  
625 calcite mesocrystals: A coordination chemistry approach. *J. Am. Chem. Soc.* 134,  
626 1367-1373.

627 Liang, Z., Li, W., Yang, S., Du, P., 2010. Extraction and structural characteristics of  
628 extracellular polymeric substances (EPS), pellets in autotrophic nitrifying  
629 biofilm and activated sludge. *Chemosphere* 81(5), 626-632.

630 Lippmann, F., 1973. Crystal chemistry of sedimentary carbonate minerals, *Sedimentary  
631 Carbonate Minerals*. Springer, pp. 5-96.

632 Liu, D., Yu, N., Papineau, D., Fan, Q., Wang, H., Qiu, X., She, Z., Luo, G., 2019a. The  
633 catalytic role of planktonic aerobic heterotrophic bacteria in protodolomite  
634 formation: Results from Lake Jibuhulangtu Nuur, Inner Mongolia, China.  
635 *Geochim. Cosmochim. Acta* 263, 31-49.

636 Liu, D., Xu, Y., Papineau, D., Yu, N., Fan, Q., Qiu, X., Wang, H., 2019b. Experimental  
637 evidence for abiotic formation of low-temperature protodolomite facilitated by  
638 clay minerals. *Geochim. Cosmochim. Acta* 247, 83-95. Loste, E., Wilson, R.M.,

639 Seshadri, R., Meldrum, F.C., 2003. The role of magnesium in stabilising  
640 amorphous calcium carbonate and controlling calcite morphologies. *J. Cryst.*  
641 *Growth* 254, 206-218.

642 Malone, M.J., Baker P.A., Burns S.J., 1996. Recrystallization of dolomite: An  
643 experimental study from 50-200°C. *Geochim. Cosmochim. Acta* 60(12), 2189-  
644 2207.

645 McCormack, J.B., Bontognali, T.R.R., Immenhauser, A., Kwiecien, O., 2018. Controls  
646 on cyclic formation of Quaternary early diagenetic dolomite. *Geophy. Res. Lett.*  
647 45, 3625-3634.

648 McKenzie, J.A., Vasconcelos, C., 2009. Dolomite Mountains and the origin of the  
649 dolomite rock of which they mainly consist: historical developments and new  
650 perspectives. *Sedimentology* 56, 205-219.

651 Meister, P., Reyes, C., Beaumont, W., Rincon, M., Collins, L., Berelson, W., Stott, L.,  
652 Corsetti, F., Nealson, K.H., 2011. Calcium and magnesium-limited dolomite  
653 precipitation at Deep Springs Lake, California. *Sedimentology* 58, 1810-1830.

654 Morse, J.W., Wang, Q., Tsio, M.Y., 1997. Influences of temperature and Mg:Ca ratio  
655 on CaCO<sub>3</sub> precipitates from seawater. *Geology* 25(1), 85-87.

656 Omoike, A., Chorover, J., 2004. Spectroscopic study of extracellular polymeric  
657 substances from *Bacillus subtilis*: Aqueous chemistry and adsorption effects.  
658 *Biomacromolecules* 5(4), 1219-1230.

659 Oren, A., 2002. Diversity of halophilic microorganisms: Environments, phylogeny,  
660 physiology, and applications. *J. Indus. Microbiol. Biotechnol.* 28, 56-63.

661 Pan, X., Liu, J., Zhang, D., Chen, X., Song, W., Wu, F., 2010. Binding of dicamba to  
662 soluble and bound extracellular polymeric substances (EPS) from aerobic  
663 activated sludge: A fluorescence quenching study. *J. Colloid. Interf. Sci.* 345,  
664 442-447.

665 Pavlov, M., Siegbahn, P.E.M., Sandström, M., 1998. Hydration of beryllium,  
666 magnesium, calcium, and zinc ions using density functional theory. *J. Phys.*  
667 *Chem. A* 102, 219-228.

668 Perri, E., Tucker, M., 2007. Bacterial fossils and microbial dolomite in Triassic  
669 stromatolites. *Geology* 35(3), 207-210.

670 Petrash, D.A., Bialik, O.M., Bontognali, T.R.R., Vasconcelos, C., Roberts, J.A.,  
671 McKenzie, J.A., Konhauser, K.O., 2017. Microbially catalyzed dolomite  
672 formation: From near-surface to burial. *Earth-Sci. Rev.* 171, 558-582.

673 Qiu, X., Wang, H., Liu, D., Gong, L., Wu, X., Xiang, X., 2012. The physiological  
674 response of *Synechococcus elongatus* to salinity: A potential biomarker for  
675 ancient salinity in evaporative environments. *Geomicrobiol. J.* 29, 477-483.

676 Qiu, X., Wang, H., Yao, Y., Duan, Y., 2017. High salinity facilitates dolomite  
677 precipitation mediated by *Haloferax volcanii* DS52. *Earth Planet. Sci. Lett.*, 472,  
678 197-205.

679 Robus, R., Hansen, T.A., Widdel, F., 2006. Dissimilatory sulfate- and sulfur-reducing  
680 prokaryotes. In *The Prokaryotes* (Dworkin, M., Falkow, S., Rosenberg, E.,  
681 Schleifer, K.H., Stackebrandt, E., eds.), Springer, New York, 659-768.

682 Roberts, J.A., Kenward, P.A., Fowle, D.A., Goldstein, R.H., González, L.A., Moore,

683 D.S., 2013. Surface chemistry allows for abiotic precipitation of dolomite at low  
684 temperature. *Proc. Natl. Acad. Sci. U. S. A.* 110, 14540-14545.

685 Rodriguez-Blanco, J.D., Shaw, S., Benning, L.G., 2015. A route for the direct  
686 crystallization of dolomite. *Am. Mineral.* 100, 1172-1181.

687 Rodriguez-Navarro, C., Jimenez-Lopez, C., Rodriguez-Navarro, A., Gonzalez-Munoz,  
688 M.T., Rodriguez-Gallego, M., 2007. Bacterially mediated mineralization of  
689 vaterite. *Geochim. Cosmochim. Acta* 71, 1197-1213.

690 Romanek, C.S., Jiménez-López, C., Navarro, A.R., Sánchez-Román, M., Sahai, N.,  
691 Coleman, M., 2009. Inorganic synthesis of Fe-Ca-Mg carbonates at low  
692 temperature. *Geochim. Cosmochim. Acta* 73, 5361-5376.

693 Sánchez-Navas, A., Martín-Algarra, A., Rivadeneyra, M.A., Melchor, S., Martín-  
694 Ramos, J.D., 2009. Crystal-growth behavior in Ca-Mg carbonate bacterial  
695 sperulites. *Cryst. Growth Des.* 9, 2690-2699.

696 Sánchez-Román, M., Vasconcelos, C., Schmid, T., Dittrich, M., McKenzie, J.A., Zenobi,  
697 R., Rivadeneyra, M.A., 2008. Aerobic microbial dolomite at the nanometer  
698 scale: Implications for the geologic record. *Geology* 36, 879-882.

699 Sánchez-Román, M., Romanek, C.S., Fernández-Remolar, D.C., Sánchez-Navas, A.,  
700 McKenzie, J.A., Pibernat, R.M., Vasconcelos, C., 2011. Aerobic  
701 biomineralization of Mg-rich carbonates: Implications for natural environments.  
702 *Chem. Geol.* 281, 143-150.

703 Shen, Z., Liu, Y., Brown, P.E., Szlufarska, I., Xu, H., 2014. Modeling the effect of  
704 dissolved hydrogen sulfide on  $Mg^{2+}$ -water complex on dolomite {104} surfaces.

705 J. Phys. Chem. C 118, 15716-15722.

706 Shen, Z., Brown, P.E., Szlufarska, I., Xu, H., 2015. Investigation of the role of  
707 polysaccharide in the dolomite growth at low temperature by using atomistic  
708 simulations. *Langmuir* 31, 10435-10442.

709 Sommerdijk, N.A.J.M., de With, G., 2008. Biomimetic CaCO<sub>3</sub> mineralization using  
710 designer molecules and interfaces. *Chem. Rev.* 108(11), 4499-4550.

711 Stephenson, A.E., DeYoreo, J.J., Wu, L., Wu, K.J., Hoyer, J., Dove, P.M., 2008.  
712 Peptides enhance magnesium signature in calcite: Insights into origins of vital  
713 effects. *Science* 322(5902), 724-727.

714 Stumm, W., Morgan, J.J., 1996. *Aquatic Chemistry*. Wiley, New York, 1022 pp.

715 van Lith, Y., Vasconcelos, C., Warthmann, R., Martins, J., McKenzie, J., 2002. Bacterial  
716 sulfate reduction and salinity: two controls on dolomite precipitation in Lagoa  
717 Vermelha and Brejo do Espinho (Brazil). *Hydrobiologia* 485, 35-49.

718 van Lith, Y., Warthmann, R., Vasconcelos, C., McKenzie, J., 2003. Sulfate-reducing  
719 bacteria induce low-temperature Ca-dolomite and high Mg-calcite formation.  
720 *Geobiology* 1, 71-79.

721 Vasconcelos, C., McKenzie, J.A., Bernasconi, S., Grujic, D., Tiens, A.J., 1995.  
722 Microbial mediation as a possible mechanism for natural dolomite formation at  
723 low temperatures. *Nature* 377, 220-222.

724 Visscher, P.T., Reid, R.P., Bebout, B.M., Hoef, S.E., Macintyre, I.G., Thompson, J.A.,  
725 1998. Formation of lithified micritic laminae in modern marine stromatolites  
726 (Bahamas): the role of sulfur cycling. *Am. Mineral.* 83, 1482-1493.

727 Voegerl, R.S., 2014. Quantifying the carboxyl group density of microbial cell surfaces  
728 as a function of salinity: insights into microbial precipitation of low-temperature  
729 dolomite. 50p. Master's thesis. University of Kansas, Lawrence, Kansas.

730 Wacey, D., Wright, D.T., Boyce, A.J., 2007. A stable isotope study of microbial  
731 dolomite formation in the Coorong Region, South Australia. *Chem. Geol.* 24,  
732 155-174.

733 Wang, D., Wallace, A.F., De Yoreo, J.J., Dove, P.M., 2009. Carboxylated molecules  
734 regulate magnesium content of amorphous calcium carbonates during  
735 calcification. *Proc. Natl. Acad. Sci.* 106(51), 21511-21516.

736 Warren, J., 2000. Dolomite: occurrence, evolution and economically important  
737 associations. *Earth-Sci. Rev.* 52, 1-81.

738 Widdel, F., Bak, F., 1991. Gram-negative mesophilic sulfate-reducing bacteria. In *The*  
739 *prokaryotes* (eds Balows A, Trüper HG, Dworkin M, Harder W, Schleifer KH).  
740 Springer Verlag, New York, pp. 3352-3378.

741 Wright, D.T., 1999. The role of sulphate-reducing bacteria and cyanobacteria in  
742 dolomite formation in distal ephemeral lakes of the Coorong region, South  
743 Australia. *Sediment. Geol.* 126, 147-157.

744 Wright, D.T., Wacey, D., 2005. Precipitation of dolomite using sulphate-reducing  
745 bacteria from the Coorong Region, South Australia: significance and  
746 implications. *Sedimentology* 52, 987-1008.

747 Xu, J., Yan, C., Zhang, F., Konishi, H., Xu, H., Teng, H.H., 2013. Testing the cation-  
748 hydration effect on the crystallization of Ca-Mg-CO<sub>3</sub> systems. *Proc. Natl. Acad.*

749 Sci. 110(44), 17750-17755.

750 You, X., Sun, S., Zhu, J., Li, Q., Hu, W., Dong, H., 2013. Microbially mediated dolomite  
751 in Cambrian stromatolites from the Tarim Basin, north-west China: implications  
752 for the role of organic substrate on dolomite precipitation. *Terra Nova* 25, 387-  
753 395.

754 Zhang, F., Xu, H., Konishi, H., Shelobolina, E.S., Roden, E., 2012a. Polysaccharide-  
755 catalyzed nucleation and growth of disordered dolomite: A potential precursor  
756 of sedimentary dolomite. *Am. Mineral.* 97, 556-567.

757 Zhang, F., Xu, H., Konishi, H., Kemp, J.M., Roden, E.E., Shen, Z., 2012b. Dissolved  
758 sulfide-catalyzed precipitation of disordered dolomite: Implications for the  
759 formation mechanism of sedimentary dolomite. *Geochim. Cosmochim. Acta* 97,  
760 148-165. Zhang, F., Xu, H., Shelobolina, E.S., Konishi, H., Converse, B., Shen,  
761 Z., Roden, E.E., 2015. The catalytic effect of bound extracellular polymeric  
762 substances excreted by anaerobic microorganisms on Ca-Mg carbonate  
763 precipitation: Implications for the “dolomite problem”. *Am. Mineral.* 100, 483-  
764 494.

765

766

767 **Figure caption:**

768 **Figure 1.** Cell density (A), solution pH (B) and alkalinity (C) versus time for the  
769 reactors inoculated with dead or live cells. (D) The concentrations of  $\text{HCO}_3^-$  and  $\text{CO}_3^{2-}$   
770 and, the yields of biomass and capsule EPS at the end of by the end of incubation.

771

772 **Figure 2.** The properties of capsule EPS: (A) zeta potential at different pHs; (B) organic  
773 contents; (C-D) composition of amino acids and monosaccharides.

774

775 **Figure 3.** Aqueous chemistry data versus time for all experimental reactors without or  
776 with capsule EPS: (A) pH; (B) soluble Ca; (C) soluble Mg; (D) DIC value; (E)  
777 calculated saturation index of protodolomite; (F) precipitated Mg vs. precipitated Ca.

778

779 **Figure 4.** Rietveld refined XRD patterns of solid products without (A) or with 70 mg/L  
780 capsule EPS (B). The inset SEM image shows the morphology of Mg-calcites.

781

782 **Figure 5.** Characterization of protodolomites produced with 140 mg/L capsule EPS: (A)  
783 Rietveld refined XRD pattern; (B) Raman spectrum; (C-D) SEM images and EDS  
784 composition; (E) STEM-EDS element maps; (F) high resolution TEM image. The inset  
785 marked in panel D shows the high magnification of crystal surface and the inset in panel  
786 F is a SAED pattern.

787

788 **Figure 6.** FT-IR spectra showing the changes of capsule EPS before and after  $\text{Mg}^{2+}$

789 adsorption.

790

791 **Figure 7.** Optimized geometries of Mg-H<sub>2</sub>O complex (Mg(H<sub>2</sub>O)<sub>6</sub>]<sup>2+</sup>) (A) and its  
792 interaction with glutamic acid (B) and mannose (C).

793

794

795

796

797

798

799

800

801

802

803

804

805

806

807

808

809

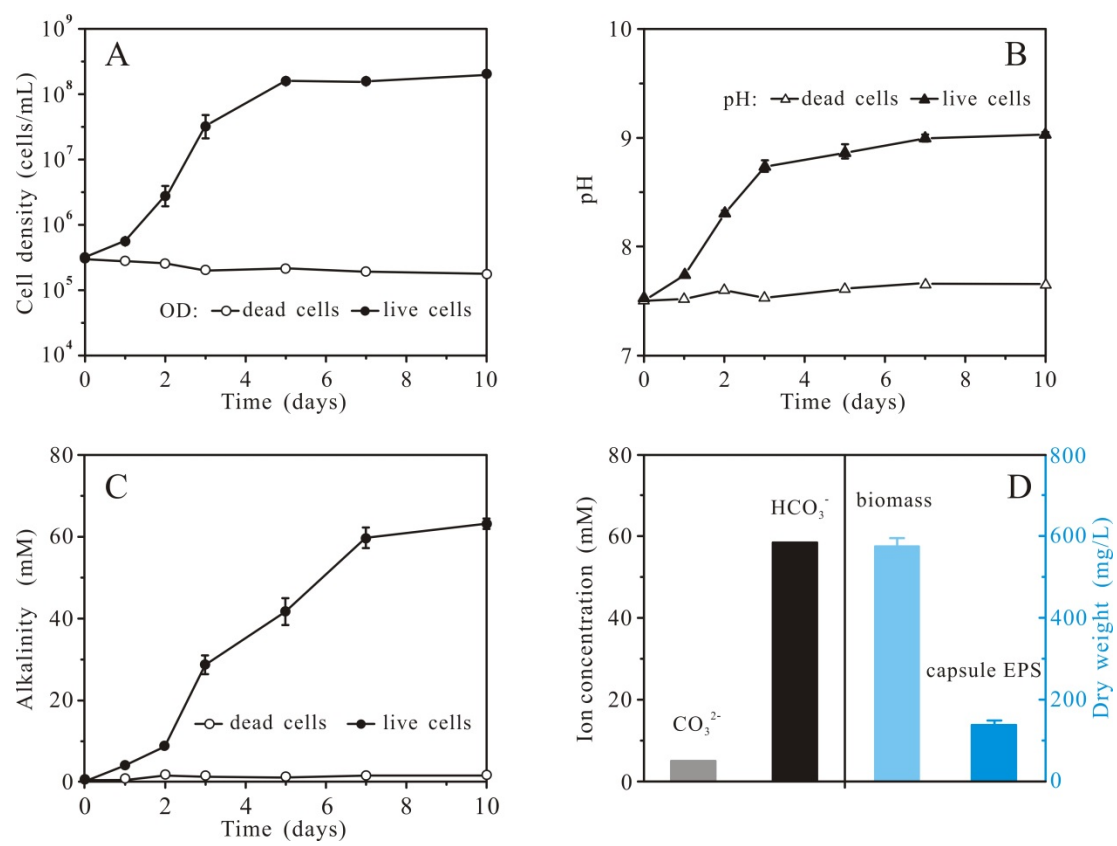


**Figure 1**

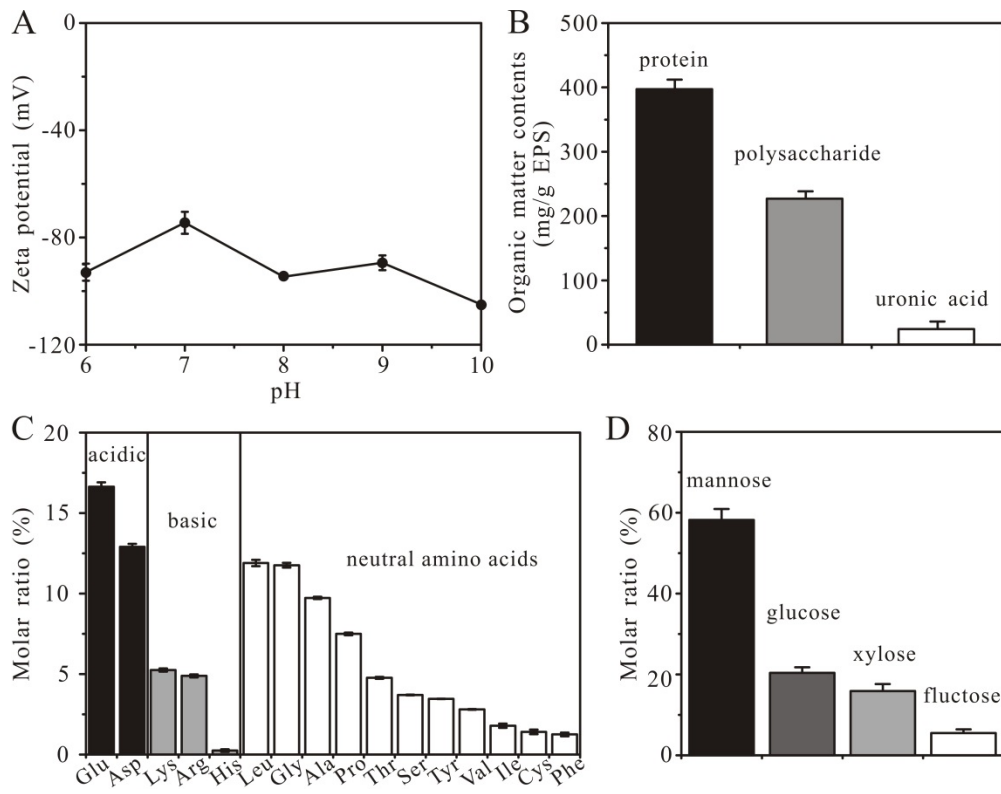


**Figure 2**

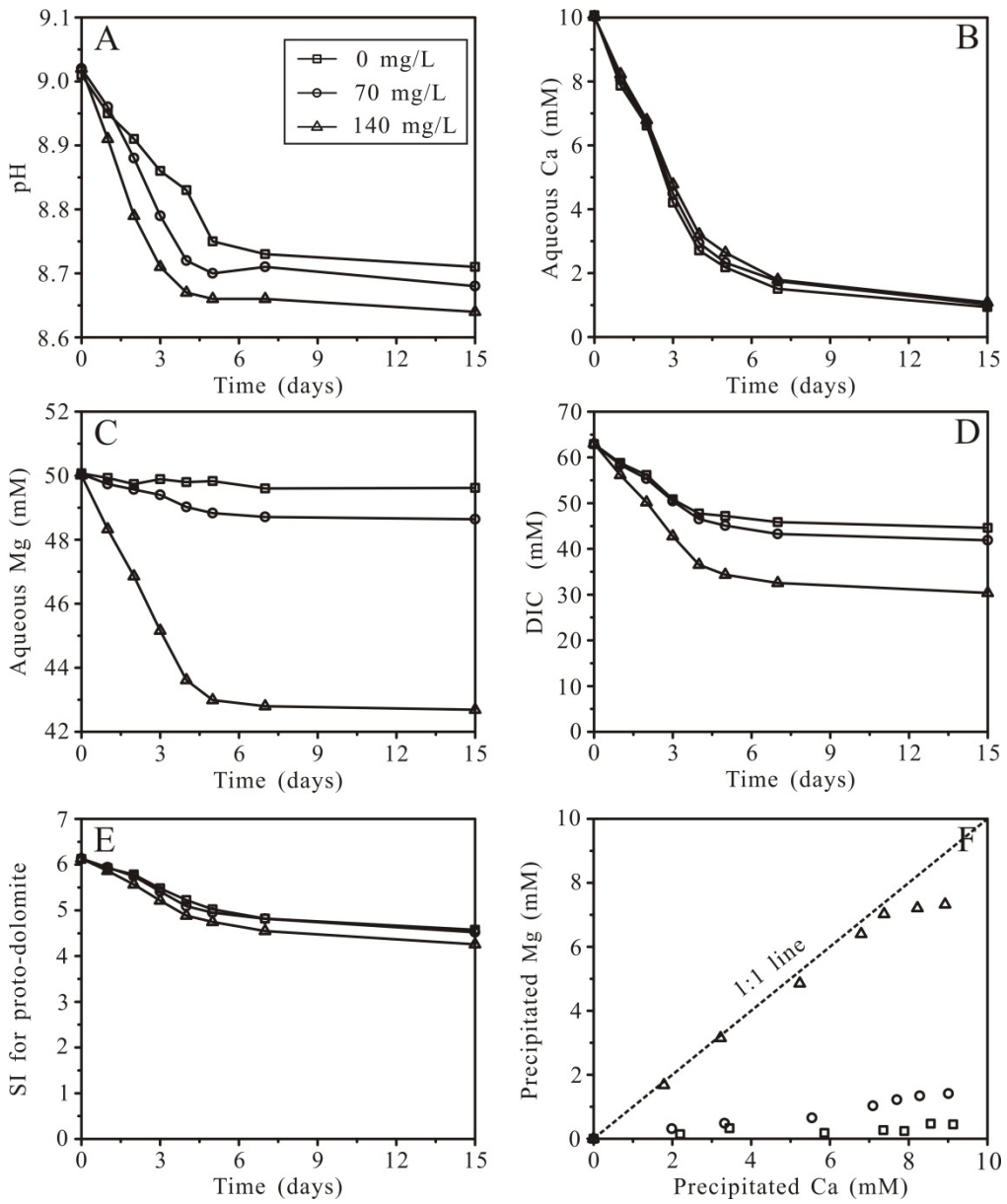


**Figure 3**

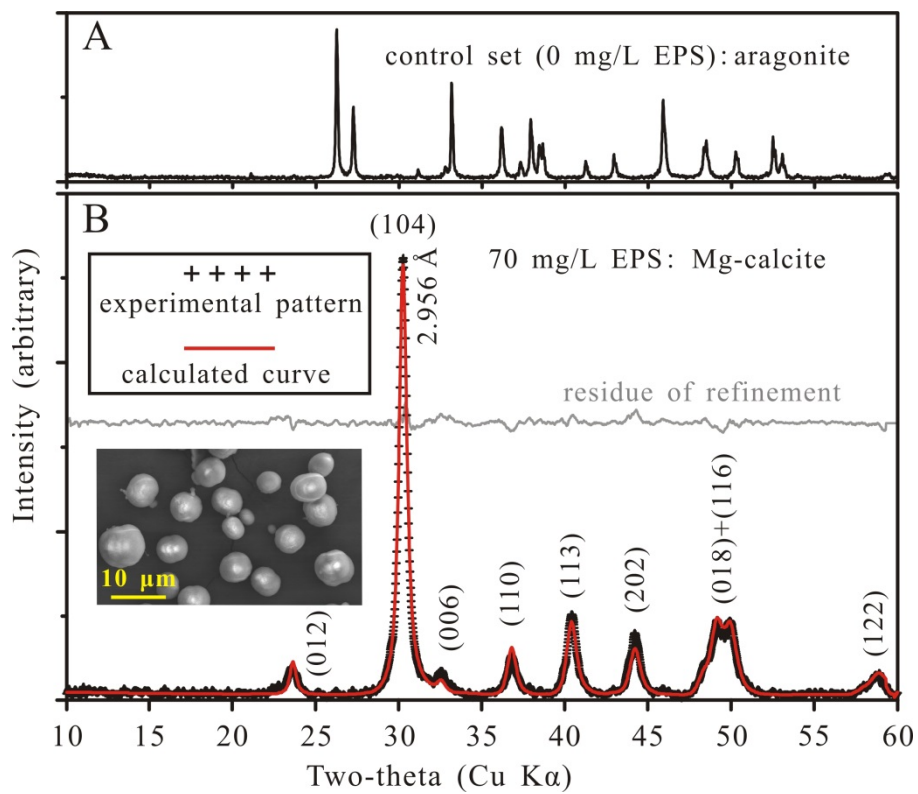


**Figure 4**

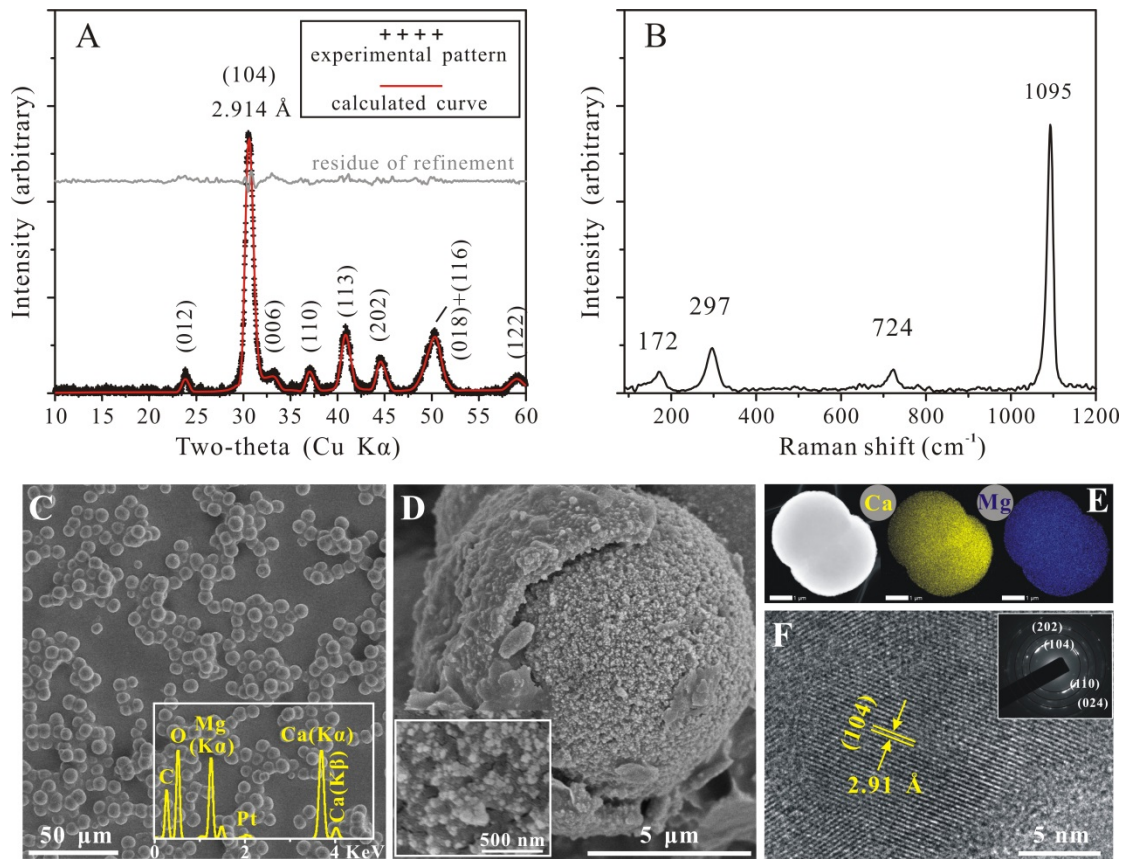


**Figure 5**

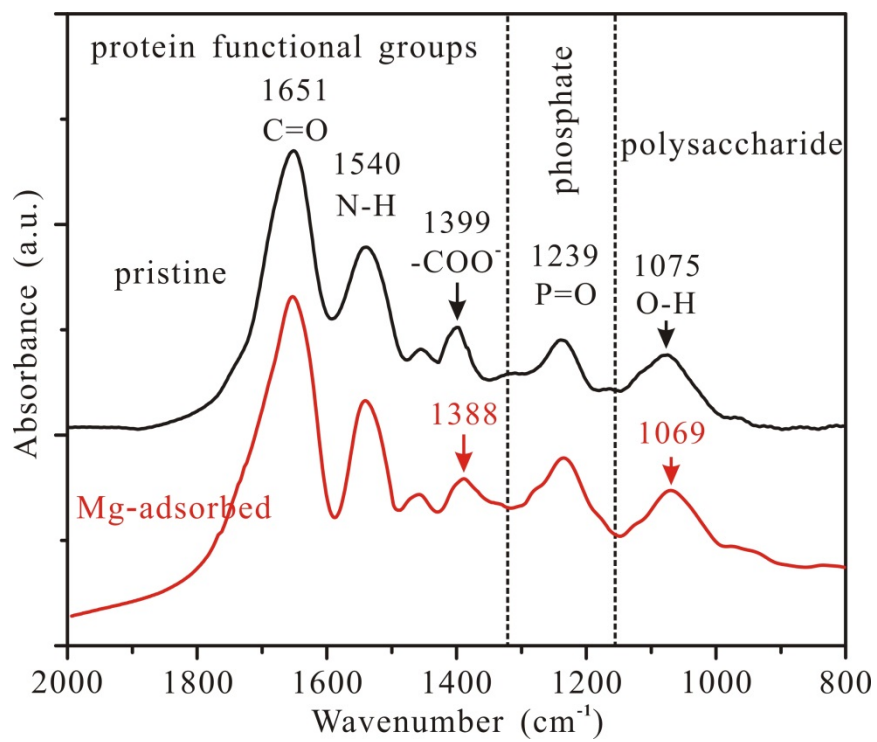


**Figure 6**

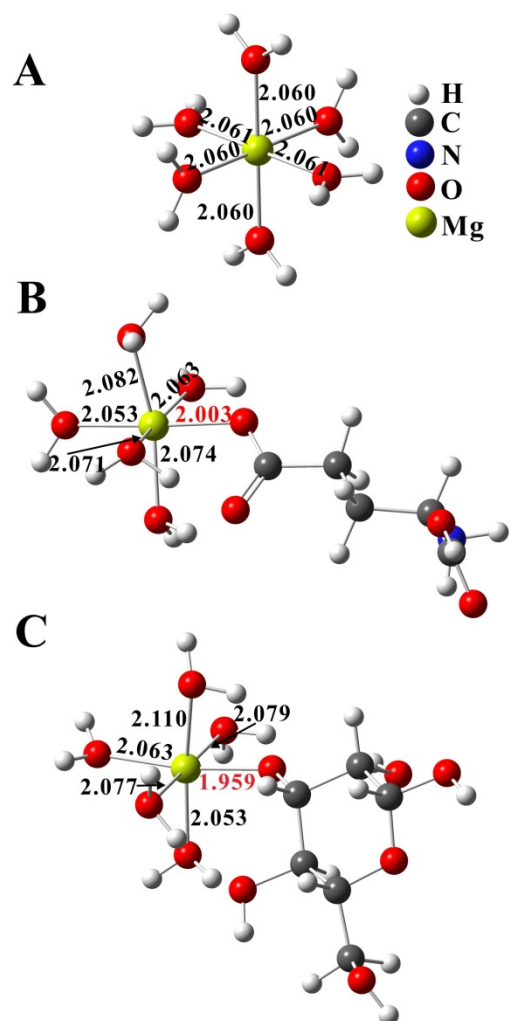


**Figure 7**